

# 3D Flexible Needle Steering in Soft-Tissue Phantoms using Fiber Bragg Grating Sensors

Momen Abayazid, Marco Kemp and Sarthak Misra

MIRA-Institute for Biomedical Technology and Technical Medicine, University of Twente, The Netherlands

**Abstract**—Needle insertion procedures are commonly used for surgical interventions. In this paper, we develop a three-dimensional (3D) closed-loop control algorithm to robotically steer flexible needles with an asymmetric tip towards a target in a soft-tissue phantom. Twelve Fiber Bragg Grating (FBG) sensors are embedded on the needle shaft. FBG sensors measure the strain applied on the needle during insertion. A method is developed to reconstruct the needle shape using the strain data obtained from the FBG sensors. Four experimental cases are conducted to validate the reconstruction method (single-bend, double-bend, 3D double-bend and drilling insertions). In the experiments, the needle is inserted 120 mm into a soft-tissue phantom. Camera images are used as a reference for the reconstruction experiments. The results show that the mean needle tip accuracy of the reconstruction method is 1.8 mm. The reconstructed needle shape is used as feedback for the steering algorithm. The steering algorithm estimates the region that the needle can reach during insertion, and controls the needle to keep the target in this region. Steering experiments are performed for 110 mm insertion, and the mean targeting accuracy is 1.3 mm. The results demonstrate the capability of using FBG sensors to robotically steer needles.

## I. INTRODUCTION

Needle insertion into soft tissue is one of the most common minimally invasive surgical procedures. Needles are often used for diagnostic and therapeutic applications such as biopsy and brachytherapy, respectively. Imaging modalities such as ultrasound and magnetic resonance (MR) images, and computed tomography (CT) scans are commonly used during needle insertion procedures to localize the needle and target for accurate tip placement. Inaccurate needle placement might cause misdiagnosis during biopsy, and unsuccessful treatment during brachytherapy. Rigid needles are used in such procedures, but they do not provide the clinician with sufficient steering capabilities to reach the target [1].

Flexible needles were introduced to facilitate curved paths to reach the target accurately. They can be used to avoid sensitive tissue that might be located along the path to the target [2], [3], [4]. Flexible needles with an asymmetric tip (e.g., bevel tip) naturally bend during insertion into soft tissue [5], [6]. Needle deflections due to tip-asymmetry can be used during insertion to steer the needle to reach a target [1], [3].

Recent studies have presented models for needle steering in two-dimensional (2D) space. DiMaio and Salcudean developed a control and path planning algorithm that relates the needle base (outside the soft-tissue phantom) motion to

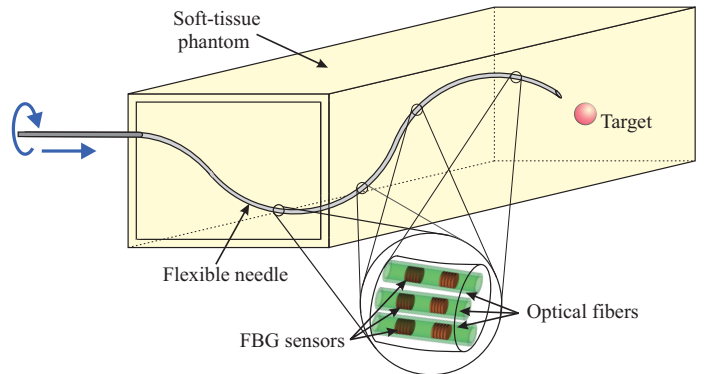


Fig. 1: Fiber Bragg Grating (FBG) sensors are used to reconstruct the needle shape during insertion into a soft-tissue phantom. Twelve FBG sensors are located on three optical fibers along the needle shaft. The reconstructed needle shape is used as feedback for the steering algorithm. Steering is accomplished by rotating the needle about its axis at the base.

the tip motion inside the tissue [7]. Glozman and Shoham presented an image-guided closed-loop control for steering flexible needles [8]. Fluoroscopic images were used for real-time feedback of the needle position. They modeled the flexible needle as a beam supported by virtual springs. Forward and inverse kinematics of the needle were solved for path planning. Neubach and Shoham, and Abayazid *et al.* used ultrasound images for tracking the tip position as feedback for 2D steering [9], [10]. Duindam *et al.* developed a model that describes three-dimensional (3D) deflection of bevel-tipped flexible needles. They used the model for path planning to steer the needle towards the target [11]. Hauser *et al.* developed a 3D feedback controller that steers the needle along a helical path [12]. The results of Duindam *et al.* and Hauser *et al.* were based on simulations, and experiments were not conducted for validation of the algorithms.

A needle tracking algorithm is required to provide the system with feedback for closed-loop control. Needle tracking techniques were developed based on ultrasound and fluoroscopic image segmentation to determine the needle shape during the insertion procedure [8], [9], [10]. The spatial resolution of 3D ultrasound images is limited [13], and the use of x-ray-based imaging (CT or fluoroscopy) exposes the patient to high doses of radiation [14]. MR imaging suffers from low refresh rate and incompatibility with magnetic materials [15]. Electromagnetic position tracking sensors [1], [16] are also used for needle tracking, but its accuracy is sensitive to ferromagnetic materials in the range of measurement. Fiber Bragg Grating (FBG) sensors can be an alternative for real-

This work was supported by funds from the Netherlands Organization for Scientific Research (NWO).

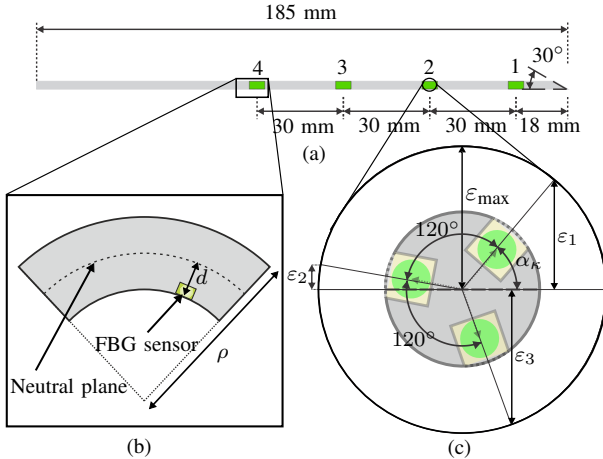


Fig. 2: Configuration of Fiber Bragg Grating (FBG) sensors on the needle. (a) The numbers 1, 2, 3 and 4 represent the sensor locations on the needle shaft. (b) The inset (left) depicts a curved needle with radius of curvature ( $\rho$ ), and the distance between the FBG sensor and the neutral plane is  $d$ . (c) The inset (right) shows the strains ( $\varepsilon_1$ ,  $\varepsilon_2$ ,  $\varepsilon_3$ ) measured by three FBG sensors. The measured strains are used to calculate the bending strain in the needle (magnitude ( $\varepsilon_{\max}$ ) and direction ( $\alpha_\kappa$ )) at a sensor location.

time 3D shape reconstruction. FBG sensors are optical sensors that can measure strain [17], [18]. The use of FBG-based needle shape reconstruction for medical applications has been shown in [19], [20], [21], [22], [23], [24].

In the current study, an algorithm is developed to robotically steer flexible needles in 3D space (Fig. 1). The steering algorithm estimates the region that the needle tip can reach during insertion in real-time. The needle rotates about its axis to keep the target in this reachable region. The needle radius of curvature, tip position and orientation are the inputs to the steering algorithm during insertion. The steering algorithm is validated by conducting insertion experiments into a soft-tissue phantom. Real-time 3D needle shape reconstruction using FBG sensors provides feedback for the steering algorithm. To the best of our knowledge, the use of FBG sensors for real-time shape reconstruction, and using this data for 3D steering of a bevel-tipped flexible needle (undergoing multiple bends) inserted into soft-tissue phantoms have not been investigated. Further, we also demonstrate the feasibility of the reconstruction method in biological tissue by conducting experiments in chicken breast.

This paper is organized as follows: Section II explains the methods used for needle shape reconstruction. Section III describes the technique used for 3D flexible needle steering. Section IV discusses the experimental setup. The experimental results and validation are provided in Section V, followed by discussion and recommendations for future work (Section VI).

## II. THREE-DIMENSIONAL NEEDLE SHAPE RECONSTRUCTION

This section describes FBG sensors integrated on the flexible needle, and the method used for 3D needle shape reconstruction.

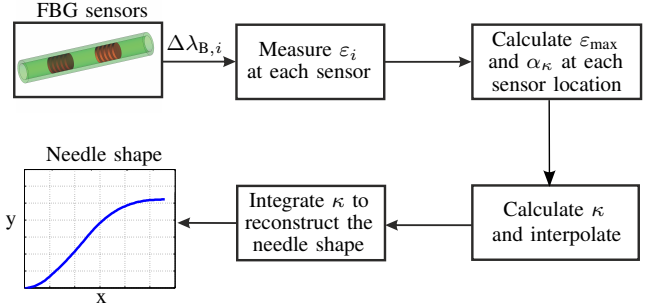


Fig. 3: The flowchart indicates the steps for needle shape reconstruction using Fiber Bragg Grating (FBG) sensors. Strains ( $\varepsilon_i$ ) are calculated according to the wavelength shifts ( $\Delta\lambda_{B,i}$ ) measured by the FBG sensors ( $i=1,\dots,12$ ). The bending strain ( $\varepsilon_{\max}$ ) and its direction ( $\alpha_\kappa$ ) at each sensor locations are interpolated to obtain the magnitude ( $\kappa$ ) and direction ( $\alpha_\kappa$ ) of the curvature function. The curvature function is integrated twice to determine the entire needle shape.

### A. Fiber Bragg Grating Sensors

An FBG sensor consists of gratings etched periodically on an optical fiber. The gratings reflect a certain wavelength ( $\lambda_B$ ) of light (Bragg wavelength), which is calculated as [17]

$$\lambda_B = 2n_{eff}\Lambda, \quad (1)$$

where  $n_{eff}$  and  $\Lambda$  are the effective refractive index and period of the grating, respectively. Mechanical strain and temperature affect the refractive index and the grating period of the sensor. In this study, we assume that FBG sensors are used at constant temperature. Applying strain on sensors causes shift in the wavelength of the reflected light ( $\Delta\lambda_B$ ). The relation between the strain ( $\varepsilon_i$ ) applied on each sensor ( $i$ ) and  $\Delta\lambda_B$  (at constant temperature) is given by [17], [25]

$$\varepsilon_i = \frac{1}{\lambda_B(1 - P_\varepsilon)} \Delta\lambda_B + \varepsilon_{T,B}, \quad (2)$$

where  $\varepsilon_{T,B}$  is the offset in the measured strain due to temperature and Bragg wavelength, and  $P_\varepsilon$  is the photo-elastic coefficient of the optical fiber. The strain measured at each sensor is used to calculate the magnitude and direction of the needle curvature.

### B. Needle Curvature Calculation

In this study, we have three fibers embedded on the needle. Four FBG sensors are placed along each fiber. The configuration of the FBG sensors along the needle and at each sensor location is shown in Fig. 2(a). This configuration of sensors is used to measure the needle curvature. The relation between the needle curvature ( $\kappa$ ) at a sensor location and the magnitude of the bending strain ( $\varepsilon_{\max}$ ) is [26]

$$\varepsilon_{\max} = \frac{d}{\rho} = d \cdot \kappa, \quad (3)$$

where  $d$  is the distance between the sensor and the neutral plane, and  $\rho$  is the radius of curvature of the needle at the sensor location (Fig. 2(b)).

The strain ( $\varepsilon_i$ ) measured by each sensor ( $i$ ) at a single location is calculated as [24]

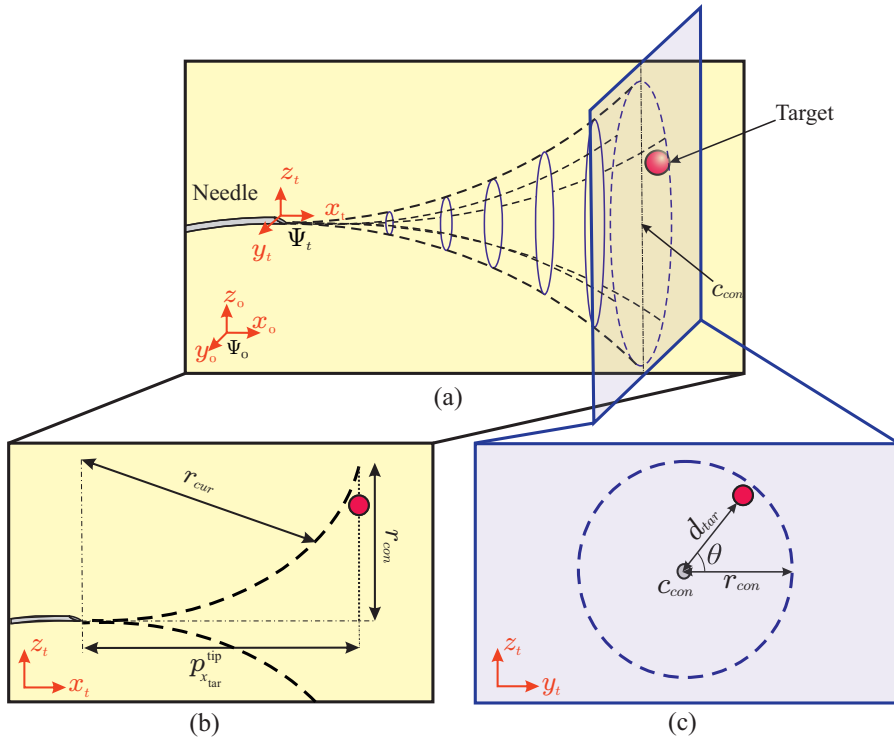


Fig. 4: The region the needle tip can reach is represented by a conical shape. (a) The frame ( $\Psi_t$ ) is attached to the needle tip, and the needle is inserted in the  $x_t$ -direction. The control circle with centre ( $c_{con}$ ) intersects the target and is perpendicular to the  $x_t$ -axis. (b) The radius ( $r_{con}$ ) is determined using the radius of curvature ( $r_{cur}$ ) of the needle and the distance ( $p_{x_{tar}}^{\text{tip}}$ ) between the tip and target along the  $x_t$ -axis. (c) The needle rotates about its axis by angle ( $\theta$ ) if the distance ( $d_{tar}$ ) between  $c_{con}$  and target is larger than or equal to  $r_{con}$ .

$$\begin{aligned}\varepsilon_1 &= \varepsilon_{T,B} + \sin(\alpha_\kappa) \cdot \varepsilon_{\max}, \\ \varepsilon_2 &= \varepsilon_{T,B} + \sin(\alpha_\kappa + 120^\circ) \cdot \varepsilon_{\max}, \\ \varepsilon_3 &= \varepsilon_{T,B} + \sin(\alpha_\kappa + 240^\circ) \cdot \varepsilon_{\max},\end{aligned}\quad (4)$$

where  $\alpha_\kappa$  is the direction of the bending strain. By solving (3) and (4), we obtain the needle curvature and its direction at each sensor location (Fig. 2(c)).

### C. Needle Shape Reconstruction

Needle shape reconstruction requires calculation of the curvature along the total inserted length. The magnitude and direction of the needle curvature at the four sensor locations (along the needle shaft) are used to reconstruct the needle shape. K-nearest neighbor interpolation algorithm is used to generate the continuous needle curvature function [27], [28]. It is assumed that the needle moves along a curved path with a constant radius. For small needle deflection, the curvature is calculated by integrating its function twice with respect to the insertion distance [29]. The needle is inserted perpendicular to the surface of the soft-tissue phantom (i.e., the slope and deflection of the needle at the insertion point are assumed to be zero). The flowchart in Fig. 3 describes the needle shape reconstruction method. Real-time needle shape reconstruction using FBG sensors is used as feedback for steering.

## III. THREE-DIMENSIONAL NEEDLE STEERING ALGORITHM

In this section, we discuss the closed-loop control algorithm for steering a bevel-tipped flexible needle towards a target in 3D. The bevel-tipped needle is assumed to move along

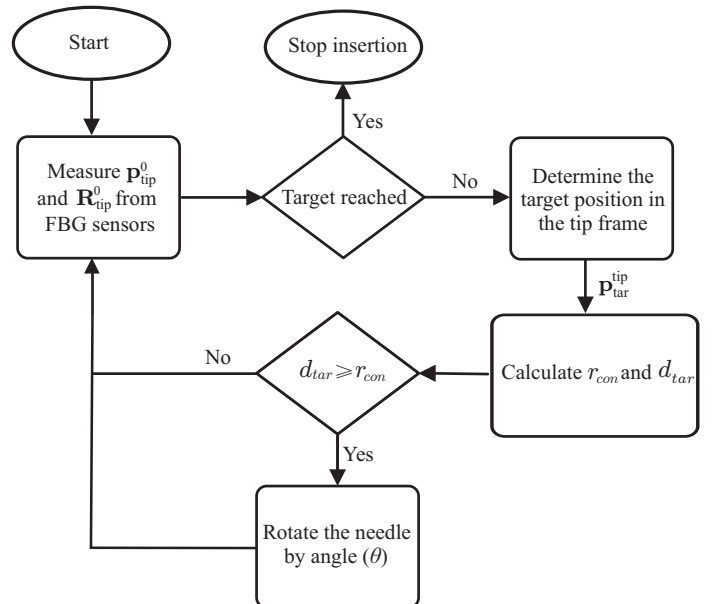


Fig. 5: The flowchart depicts the control algorithm used for needle steering. The needle tip position ( $p_{\text{tip}}^0$ ) and orientation ( $R_{\text{tip}}^0$ ) are obtained from the reconstruction algorithm (Section II-C). The target position ( $p_{\text{tar}}^{\text{tip}}$ ) with respect to the tip frame is determined. The distance between the centre ( $c_{\text{con}}$ ) of the control circle (with radius ( $r_{\text{con}}$ )) and target is  $d_{\text{tar}}$ . If  $d_{\text{tar}} \geq r_{\text{con}}$ , the needle will rotate about its axis by the angle ( $\theta$ ).

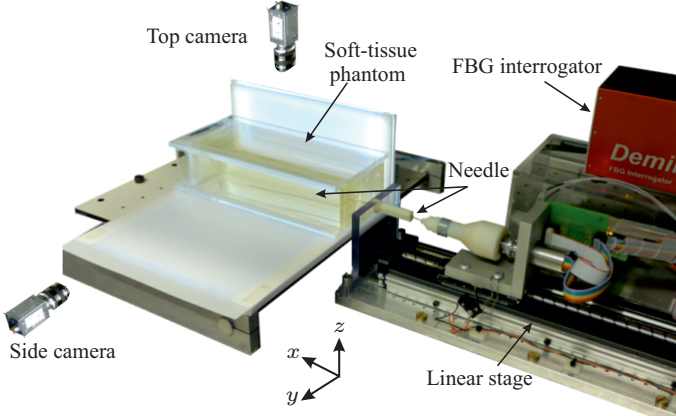


Fig. 6: Needle steering setup: A linear stage is used to insert the Nitinol needle (integrated with Fiber Bragg Grating (FBG) sensors) into a soft-tissue phantom. The needle shape is reconstructed using FBG sensors connected to an interrogator. Two charge-coupled device cameras (top and side) are used as reference for validation.

a circular path during insertion [5], [6]. Additionally, the soft-tissue phantom is assumed to be stiff enough to support the needle shaft to follow the path created by the needle. The direction of the circular path depends on the orientation of the bevel tip. The bevel tip orientation is controlled by needle rotation about its insertion axis at the base. This rotation enables the steering algorithm to direct the tip towards the target.

The steering algorithm assumes that frame ( $\Psi_t$ ) is attached to the needle tip (Fig. 4(a)). The algorithm obtains the needle tip position ( $\mathbf{p}_{\text{tip}}^0$ ) and orientation ( $\mathbf{R}_{\text{tip}}^0$ ) with respect to the global coordinate frame ( $\Psi_0$ ) using the reconstruction algorithm (Section II-C). The target position is set to be a static point in 3D space. The target position ( $\mathbf{p}_{\text{tar}}^{\text{tip}}$ ) with respect to frame ( $\Psi_t$ ) is

$$\mathbf{p}_{\text{tar}}^{\text{tip}} = [ p_{x_{\text{tar}}}^{\text{tip}} \quad p_{y_{\text{tar}}}^{\text{tip}} \quad p_{z_{\text{tar}}}^{\text{tip}} ]^T, \quad (5)$$

where  $p_{x_{\text{tar}}}^{\text{tip}}$ ,  $p_{y_{\text{tar}}}^{\text{tip}}$  and  $p_{z_{\text{tar}}}^{\text{tip}}$  are target positions along the  $x_t$ -,  $y_t$ - and  $z_t$ -axes, respectively. The region that the needle can reach in 3D is represented by a conical shape shown in Fig. 4(a). The plane of the control circle with centre ( $c_{\text{con}}$ ) intersects the target and lies on the plane perpendicular to the  $x_t$ -axis. The radius ( $r_{\text{con}}$ ) of the control circle is calculated using

$$r_{\text{con}} = r_{\text{cur}} - \sqrt{r_{\text{cur}}^2 - (p_{x_{\text{tar}}}^{\text{tip}})^2}, \quad (6)$$

where  $r_{\text{cur}}$  is the radius of curvature of the needle path (Fig. 4(b)), and it is obtained from experiments. The distance between  $c_{\text{con}}$  and the target position in  $y_t z_t$ -plane (Fig. 4(c)) is determined using

$$d_{\text{tar}} = \sqrt{(p_{z_{\text{tar}}}^{\text{tip}})^2 + (p_{y_{\text{tar}}}^{\text{tip}})^2}. \quad (7)$$

The radius ( $r_{\text{con}}$ ) decreases during insertion as the needle moves towards the target. If the control circle does not intersect the target ( $d_{\text{tar}} \geq r_{\text{con}}$ ), the needle will rotate about its axis to keep the needle in the reachable region. The needle rotates by the angle ( $\theta$ ) to direct the needle tip towards the target (Fig. 4(c)), and  $\theta$  is calculated as

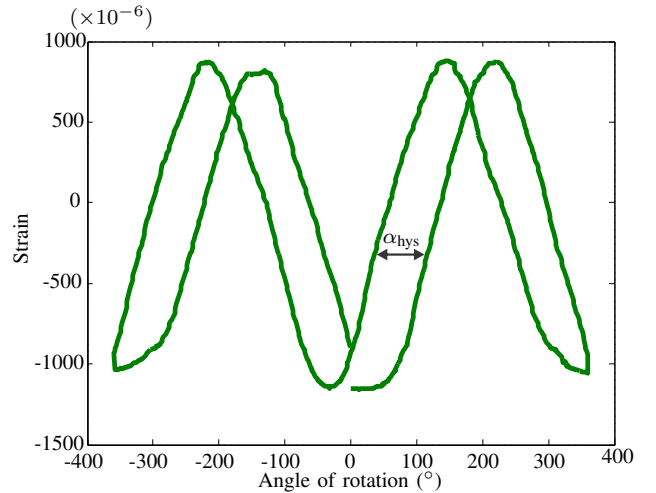


Fig. 7: The plot shows strain measurements obtained from the Fiber Bragg Grating sensor location 1 (Fig 2). The hysteresis angle ( $\alpha_{\text{hys}}$ ) is illustrated when needle rotates about its axis 360° clockwise and counterclockwise, and then back to its original orientation at 30°/s. The measured  $\alpha_{\text{hys}}$  at this found to be  $74 \pm 6^\circ$ .

$$\theta = \tan^{-1} \left( \frac{p_{z_{\text{tar}}}^{\text{tip}}}{p_{y_{\text{tar}}}^{\text{tip}}} \right). \quad (8)$$

The flowchart in Fig. 5 describes the steering algorithm. The steering algorithm is implemented, and experiments are conducted for validation in the following section.

#### IV. EXPERIMENTS

This section presents the needle design and the location of the FBG sensors on the needle. The experimental setup used to insert the needle into the soft-tissue phantom is discussed, and the validation of the reconstruction method is also provided.

##### A. Experimental Setup

The needle is mounted in a two degrees-of-freedom (DOF) insertion device (Fig. 6). The two-DOF device allows the needle to be inserted and rotated about its axis. The details of the experimental setup are presented in [30], [31].

The needle is inserted into a soft-tissue phantom made up of a gelatin mixture [31]. The needle has a total length of 185 mm. The flexible needle is made of Nitinol alloy (nickel and titanium). The Nitinol needle has a diameter of 1.0 mm with a bevel angle (at the tip) of 30°. FBG sensors are placed at four locations along the needle shaft (Fig. 2(a)). At each sensor location, three FBG sensors are placed 120° apart (Fig. 2(c)). This enables us to measure the magnitude and direction of curvature (4). The sensors are connected to a Deminsys Pyton interrogator (Technobis, Uitgeest, The Netherlands). The interrogator measures the reflected wavelength for each FBG sensor at rate of 20 kHz. The data from the FBG sensors is transferred to a computer via an ethernet cable. The computer receives the sensor data as UDP-packets using C++.

##### B. Hysteresis Calibration of the Fiber Bragg Grating Sensors

Calibration is applied for torsional compensation. Friction along the needle shaft during rotation around its axis results in

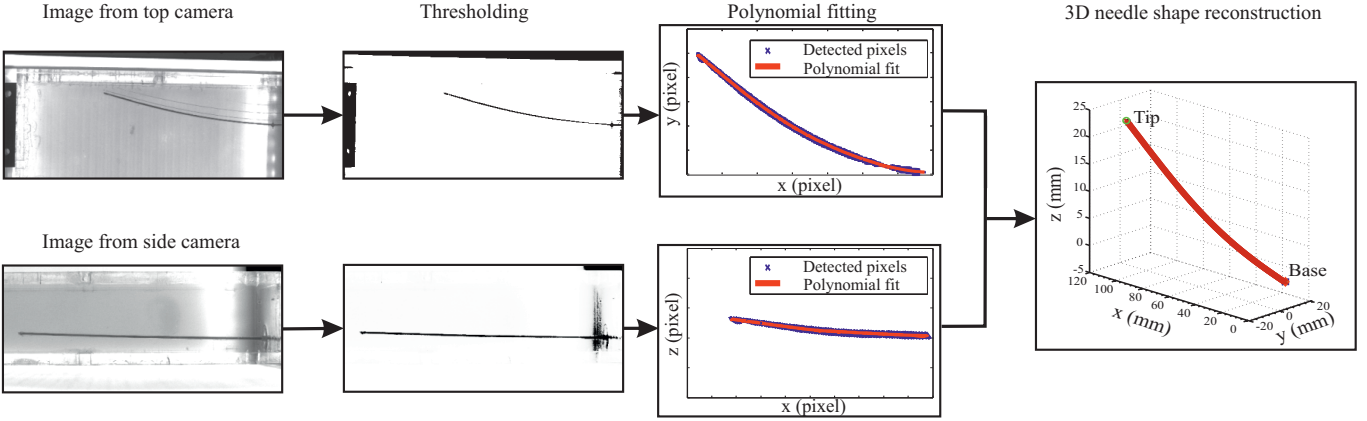


Fig. 8: Top and side camera images are used to validate the reconstruction method. Thresholding is applied on images obtained from both cameras. The pixels that represent the needle shape are localized. A polynomial is fit to the pixel positions. The resulting curves from both camera images are used to reconstruct the needle shape in three-dimensional space.

a difference between the rotation angle applied at the needle base and the orientation angle at the tip. This difference in the rotation angle (hysteresis angle ( $\alpha_{\text{hys}}$ )) is measured experimentally. In the calibration experiments, the needle is inserted 120 mm in the soft-tissue phantom, and then the needle rotates 360° with an angular velocity of 30°/s in both directions (clockwise and counterclockwise) as shown in Fig. 7. The hysteresis is calibrated for the four sensor locations along the needle. The calibration experiments show that at sensor locations 1, 2, 3 and 4 (Fig. 2(a)), the angles ( $\alpha_{\text{hys}}$ ) are found to be 74±6°, 70±7°, 62±9° and 51±7°, respectively. The data from the calibrated FBG sensors are used for the needle shape reconstruction method (Section II). By solving (4) to calculate  $\alpha_{\kappa}$  and measuring the hysteresis effect ( $\alpha_{\text{hys}}$ ), the calibrated direction of curvature of the needle ( $\alpha_{\kappa,\text{cal}}$ ) is calculated as [32]

$$\alpha_{\kappa,\text{cal}} = \alpha_{\kappa} + \alpha_{\text{rot}} \pm \frac{\alpha_{\text{hys}}}{2}, \quad (9)$$

where  $\varepsilon_1$ ,  $\varepsilon_2$  and  $\varepsilon_3$  are the strains measured by the three sensors at a single location, and  $\alpha_{\text{rot}}$  is the rotation applied at the base of the needle. The sign of  $\alpha_{\text{hys}}$  depends on the direction of needle rotation. The needle shape reconstruction method is validated using a 3D image-based technique.

### C. Validation of the Needle Shape Reconstruction Method

The needle shape reconstruction using FBG sensors in the soft-tissue phantom is verified using two charge-coupled device (CCD) cameras (positioned at the top and the side of the soft-tissue phantom) as a reference measurement (Fig. 6). A threshold is applied on the images captured from both cameras to produce binary images (Fig. 8). The resulting image after thresholding is inverted to make the background black, and the pixels that represent the needle shape are obtained by localizing the white pixels in the images. Polynomial fitting of the localized pixels is used to produce the needle shape in each camera image. The 3D position of a pixel is calculated by selecting a matching pixel in the two camera images, as shown in Fig. 8. The algorithm used for 3D reconstruction is based on a 3D stereoscopic reconstruction

method described by Jahya *et al.* [33]. The results of the validation experiments are presented in Section V-A.

## V. RESULTS

In this section, we first present the experimental results of needle shape reconstruction using data from FBG sensors. We also conduct experiments to steer a flexible needle towards different target positions in 3D space.

### A. Needle Shape Reconstruction

The needle shape reconstruction method (Section II) is verified for the following experimental cases, where the needle is inserted at 10 mm/s (within the range of insertion velocities used in clinical applications (0.4 - 10 mm/s) [34]) and it rotates about its axis at 30°/s:

- (i) Single-bend: Needle is inserted 120 mm, with no rotation.
- (ii) Double-bend: Needle is inserted 120 mm, with 180° rotation at: (a) 40 mm, (b) 60 mm and (c) 80 mm insertion distance.
- (iii) 3D double-bend: Needle is inserted 120 mm, with 90° rotation at: (a) 40 mm, (b) 60 mm and (c) 80 mm insertion distance.
- (iv) Drilling: Needle rotates continuously (drilling motion) for the first: (a) 40 mm, (b) 60 mm and (c) full 120 mm insertion. This is followed by a single-bend insertion.

Each experimental case is repeated six times. The results of needle reconstruction experiments are shown in Fig. 9. The final needle shape is also determined using camera images to validate the reconstruction method. The difference ( $e_{\text{tip}}$ ) between the tip position ( $x$ -,  $y$ - and  $z$ -coordinates) obtained using FBG sensors and camera images is calculated as

$$e_{\text{tip}} = \| \mathbf{p}_{\text{FBG}} - \mathbf{p}_{\text{cam}} \|, \quad (10)$$

where  $\mathbf{p}_{\text{FBG}}$  and  $\mathbf{p}_{\text{cam}}$  are the tip positions measured using FBG sensors and camera images, respectively. The maximum mean tip error is 2.1 ± 1.1 mm, and is observed for the 3D double-bend case.

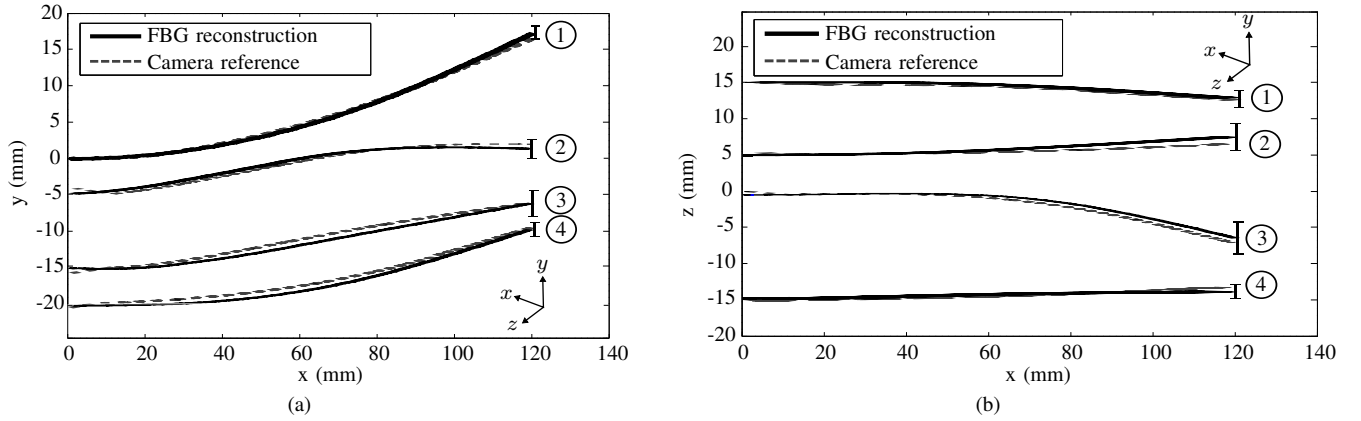


Fig. 9: Needle shape reconstruction ((a) top view and (b) side view) for insertion into a soft-tissue phantom: ① Single-bend (mean tip error ( $e_{tip}$ ) is  $1.5 \pm 0.8$  mm). ② Double-bend ( $e_{tip}$  is  $2.0 \pm 0.7$  mm). ③ Three-dimensional double-bend ( $e_{tip}$  is  $2.1 \pm 1.1$  mm). ④ Drilling ( $e_{tip}$  is  $1.7 \pm 1.2$  mm). Each experiment is repeated six times.

### B. Needle Steering

The data obtained from FBG sensors are used as feedback for closed-loop needle steering as described in Section III. The radius of curvature ( $r_{cur}$ ) of the needle is determined experimentally from the single-bend experiments by fitting the needle shape to a circle and calculating the radius of the fitted circle. The value of  $r_{cur}$  used in the steering experiments is 375 mm. In the experiments, the target is positioned initially in the reachable region of the needle. The needle can rotate in both directions to reduce the effect of needle torsion in the soft-tissue phantom. Hysteresis calibration is performed online before every rotation during the steering experiments. Experiments are conducted to steer the needle towards four different target positions. The target positions and reconstructed needle shapes during steering experiments are shown in Fig. 10. Three steering experiments are performed for each target position. The mean targeting error is calculated as  $\|\mathbf{p}_{tip} - \mathbf{p}_{tar}\|$ , where  $\mathbf{p}_{tip}$  is the tip position and  $\mathbf{p}_{tar}$  is the target position. The needle shape is also reconstructed using camera images for validation. The results show that the mean targeting error ( $e_{tip}$ ) measured using the FBG sensors and camera images are  $1.2 \pm 0.5$  mm and  $1.3 \pm 0.9$  mm, respectively.

## VI. DISCUSSION

In this study, a 3D needle steering algorithm is developed to steer a flexible needle towards a target. The steering algorithm uses 3D needle shape as feedback from the FBG sensors. Twelve FBG sensors are embedded on a 1.0 mm diameter flexible Nitinol needle. The needle bending strain is measured at four locations along the needle shaft. 3D needle curvature is derived from the measured strains. K-nearest neighbor interpolation is used to estimate the curvature along the entire needle.

Hysteresis calibration is also applied to estimate difference between the needle orientation at the tip and base. This is caused by friction between the needle and the surrounding tissue during rotation about its axis. Hysteresis is compensated for by calculating the angle ( $\alpha_{hys}$ ) for accurate steering and shape reconstruction.

Needle shape is reconstructed in real-time for both in-plane and out-of-plane insertions in a soft-tissue phantom. The reconstructed needle shape using FBG sensors is validated using camera images as a reference. The errors between the 3D tip position obtained from FBG sensors and camera images are 1.5 mm, 2.0 mm, 2.1 mm and 1.7 mm for single-bend, double-bend, 3D double-bend and drilling insertions, respectively.

The steering algorithm estimates the region that the needle can reach during insertion in real-time. The needle is steered to keep the target in the reachable region. The volume of the reachable region decreases during insertion. Experiments are conducted to evaluate the steering algorithm. The needle is steered towards target positions in 3D space. The mean targeting error is 1.3 mm. These results show that FBG sensors can be combined with clinical imaging modalities or used independently for robotically steering needles. Furthermore, preliminary experiments show the feasibility of using the needle shape reconstruction method in biological tissue (*please refer to the attached video*).

The accuracy of the 3D needle shape reconstruction method can be improved if we increase the number of sensors integrated on the needle. Needle steering will be extended to include path planning algorithms to select the optimal path that the needle can follow to reach a target. Target motion in 3D space will also be tracked in real-time to increase the targeting accuracy.

## REFERENCES

- [1] N. Abolhassani, R. V. Patel, and M. Moallem, "Needle insertion into soft tissue: A survey," *Medical Engineering and Physics*, vol. 29, no. 4, pp. 413–431, 2007.
- [2] A. Grant and J. Neuberger, "Guidelines on the use of liver biopsy in clinical practice," *Journal of Gastroenterology and Hepatology*, vol. 45, no. Supplement IV, pp. IV1–IV11, 1999.
- [3] V. Kallem and N. Cowan, "Image-guided control of flexible bevel-tip needles," in *Proceedings of the IEEE International Conference on Robotics and Automation (ICRA)*, pp. 3015–3020, April 2007.
- [4] N. J. Cowan, K. Goldberg, G. S. Chirikjian, G. Fichtinger, K. B. Reed, V. Kallem, W. Park, S. Misra, and A. M. Okamura, *Surgical Robotics*, ch. Robotic Needle Steering: Design, Modeling, Planning, and Image Guidance, pp. 557–582. Springer US, 2011.

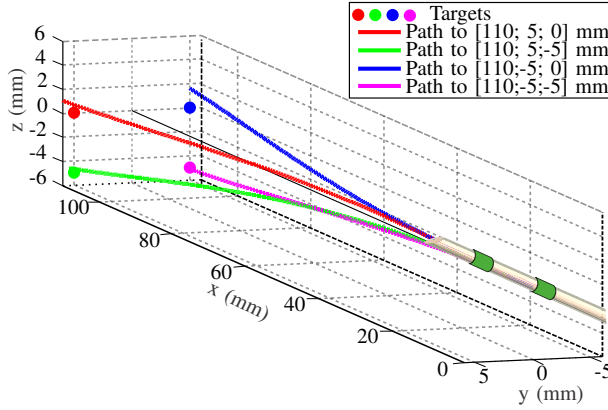


Fig. 10: Shape reconstruction results for the needle path during steering towards different target positions. The mean number of needle rotations to reach the target is 8. The mean targeting accuracy is  $1.3 \pm 0.9$  mm. Please refer to the attached video that demonstrates the results of needle steering experiments.

- [5] R. J. Webster, J. S. Kim, N. J. Cowan, G. S. Chirikjian, and A. M. Okamura, "Nonholonomic modeling of needle steering," *International Journal of Robotics Research*, vol. 25, no. 5-6, pp. 509–525, 2006.
- [6] S. Misra, K. B. Reed, B. W. Schafer, K. T. Ramesh, and A. M. Okamura, "Mechanics of flexible needles robotically steered through soft tissue," *International Journal of Robotic Research*, vol. 29, no. 13, pp. 1640–1660, 2010.
- [7] S. P. DiMaio and S. E. Salcudean, "Needle steering and model-based trajectory planning," in *Proceedings of the International Conference on Medical Image Computing and Computer-Assisted Intervention (MICCAI)*, vol. 2878, pp. 33–40, Montréal, Canada, November 2003.
- [8] D. Glzman and M. Shoham, "Image-guided robotic flexible needle steering," *IEEE Transactions on Robotics*, vol. 23, no. 3, pp. 459–467, 2007.
- [9] Z. Neubach and M. Shoham, "Ultrasound-guided robot for flexible needle steering," *IEEE Transactions on Biomedical Engineering*, vol. 57, no. 4, pp. 799–805, 2010.
- [10] M. Abayazid, R. J. Roesthuis, R. Reilink, and S. Misra, "Integrating deflection models and image feedback for real-time flexible needle steering," *IEEE Transactions on Robotics*, 2013. In Press.
- [11] V. Duindam, R. Alterovitz, S. Sastry, and K. Goldberg, "Screw-based motion planning for bevel-tip flexible needles in 3d environments with obstacles," in *Proceedings of the IEEE International Conference on Robotics and Automation (ICRA)*, pp. 2483–2488, Pasadena, CA, USA, May 2008.
- [12] K. Hauser, R. Alterovitz, N. Chentanez, A. Okamura, and K. Goldberg, "Feedback control for steering needles through 3d deformable tissue using helical paths," in *Proceedings of Robotics: Science and Systems (RSS)*, vol. 37, Seattle, USA, June 2009.
- [13] P. M. Novotny, J. A. Stoll, N. V. Vasilyev, P. J. del Nido, P. E. Dupont, T. E. Zickler, and R. D. Howe, "Gpu based real-time instrument tracking with three-dimensional ultrasound," *Medical Image Analysis*, vol. 11, no. 5, pp. 458 – 464, 2007.
- [14] H. L. Fred, "Drawbacks and limitations of computed tomography," *Texas Heart Institute Journal*, vol. 31, no. 2, pp. 345–348, 2004.
- [15] S. P. DiMaio, E. Samset, G. Fischer, I. Iordachita, G. Fichtinger, F. Jolesz, and C. M. Tempany, "Dynamic mri scan plane control for passive tracking of instruments and devices," in *Medical Image Computing and Computer-Assisted Intervention* (N. Ayache, S. Ourselin, and A. Maeder, eds.), pp. 50–58, Springer Berlin / Heidelberg, 2007.
- [16] N. D. Glossop, K. Cleary, L. Kull, and F. Banovac, "Needle tracking using the aurora magnetic position sensor," in *Proceedings Computer Assisted Orthopaedic Surgery*, pp. 90–92, Santa Fe, USA, June 2002.
- [17] A. Othonos, K. Kalli, D. Pureur, and A. Mugnier, "Fibre bragg gratings," in *Wavelength Filters in Fibre Optics*, pp. 189–269, Springer Berlin / Heidelberg, 2006.
- [18] I. Payo, V. Feliu, and O. D. Cortázar, "Fibre bragg grating (fbg) sensor system for highly flexible single-link robots," *Sensors and Actuators A: Physical*, vol. 150, no. 1, pp. 24–39, 2009.
- [19] Z. Lunwei, Q. Jinwu, S. Linyong, and Z. Yanan, "Fbg sensor devices for spatial shape detection of intelligent colonoscope," in *Proceedings of the IEEE International Conference on Robotics and Automation (ICRA)*, vol. 1, pp. 834–840, April-May 2004.
- [20] L. Zhang, J. Qian, Y. Zhang, and L. Shen, "On sdm/wdm fbg sensor net for shape detection of endoscope," in *Proceeding of the IEEE International Conference on Mechatronics and Automation*, vol. 4, pp. 1986–1991, July-August 2005.
- [21] X. Yi, J. Qian, L. Shen, Y. Zhang, and Z. Zhang, "An innovative 3d colonoscope shape sensing sensor based on fbg sensor array," in *Proceedings of the International Conference on Information Acquisition (ICIA)*, pp. 227–232, July 2007.
- [22] Y.-L. Park, S. Elayaperumal, B. Daniel, C. R. Seok, S. Mihye, J. Savall, R. Black, B. Moslehi, and M. Cutkosky, "Real-time estimation of 3-d needle shape and deflection for mri-guided interventions," *IEEE/ASME Transactions on Mechatronics*, vol. 15, no. 6, pp. 906 –915, 2010.
- [23] V. Mishra, N. Singh, U. Tiwari, and P. Kapur, "Fiber grating sensors in medicine: Current and emerging applications," *Sensors and Actuators A: Physical*, vol. 167, no. 2, pp. 279–290, 2011.
- [24] K. Henken, D. J. van Gerwen, J. Dankelman, and J. J. van den Dobbelaer, "Accuracy of needle position measurements using fiber bragg gratings," *Minimally Invasive Therapy & Allied Technologies*, vol. 21, no. 6, pp. 408–414, 2012.
- [25] K. O. Hill and G. Meltz, "Fiber bragg grating technology fundamentals and overview," *Journal of Lightwave Technology*, vol. 15, no. 8, pp. 1263–1276, 1997.
- [26] J. Gere and S. Timoshenko, *Mechanics of Materials*. Stanley Thornes, 1999.
- [27] J. H. Friedman, J. L. Bentley, and R. A. Finkel, "An algorithm for finding best matches in logarithmic expected time," *ACM Transactions on Mathematical Software*, vol. 3, no. 3, pp. 209–226, 1977.
- [28] T. Lehmann, C. Gonner, and K. Spitzer, "Survey: interpolation methods in medical image processing," *IEEE Transactions on Medical Imaging*, vol. 18, no. 11, pp. 1049–1075, 1999.
- [29] T. Megson, *Structural and Stress Analysis*. Elsevier Butterworth-Heinemann, second edition ed., 2005.
- [30] Y. R. J. van Veen, A. Jayha, and S. Misra, "Macroscopic and microscopic observations of needle insertion into gels," *Proceedings of the Institution of Mechanical Engineers, Part H: Journal of Engineering in Medicine*, vol. 226, no. 6, pp. 441–449, 2012.
- [31] R. J. Roesthuis, Y. R. J. van Veen, A. Jayha, and S. Misra, "Mechanics of needle-tissue interaction," in *Proceedings of the IEEE International Conference on Intelligent Robots and Systems (IROS)*, pp. 2557–2563, San Francisco, California, USA, September 2011.
- [32] M. Kemp, "Flexible needle steering using fiber bragg grating sensors," Master's thesis, Faculty of Electrical Engineering, Mathematics and Computer Science, University of Twente, The Netherlands, August 2012.
- [33] A. Jayha, F. van der Heijden, and S. Misra, "Observations of three-dimensional needle deflection during insertion into soft tissue," in *Proceedings of the IEEE RAS/EMBS International Conference on Biomedical Robotics and Biomechatronics (BioRob)*, pp. 1205–1210, Rome, Italy, June 2012.
- [34] S. DiMaio and S. Salcudean, "Needle insertion modelling and simulation," in *Proceedings of the IEEE International Conference on Robotics and Automation (ICRA)*, vol. 2, pp. 2098–2105, Washington, D.C., USA, May 2002.